

Dynamic Heterodyne Interferometry

Tomohiro Maeda¹, Achuta Kadambi^{1,2}, Yoav Y. Schechner³, Ramesh Raskar¹

¹MIT Media Lab

²Harvard Medical School

³Viterbi Faculty of Electrical Engineering, Technion, Israel

Abstract

Dynamic interferometry enables snapshot recovery of phase images by using polarization phase shifting. However, the phase estimate is susceptible to influence from sources of ambient light having uncontrolled polarization. We present a novel method, dynamic heterodyne interferometry (DHI), as a means to mitigate phase bias from ambient light sources, while retaining dynamic potential.

1. Introduction

Interferometry depends on the phase difference between wavefronts propagating in two paths (arms). To estimate the phase difference using intensity measurements, a wide range of techniques exists. A prevalent principle is *phase shift interferometry* [13, 34], which relies on multiple interferograms. Each interferogram uses a different and known phase shift between the two arms of the interferometer. At least three interferograms are required. Without loss of generality, this paper considers the *four phase trick*, which relies on four interferograms at quarter wavelength phase shifts [8]. However, sequential capture of multiple interferograms limits the acquisition speed of phase shift interferometry.

Parallelizing the interferogram creation can improve the speed of acquisition. This is realized by using polarized interferograms, in an approach termed *dynamic interferometry* [10, 34, 40]. Unfortunately, dynamic interferometry is susceptible to bias from partially polarized ambient light. We claim that such ambient disturbances can be reduced by using *heterodyne interferometry*, where temporal correlations occur at different phase shifts [13, 44]. In this paper, we study incorporation of heterodyne principles into the framework of dynamic interferometry. Hence, we refer to this hybrid approach as *dynamic heterodyne interferometry* (DHI). In our proposed formulation, each arm of

Table 1: Comparing the proposed approach with the closest related methods in interferometry.

	Phase Shift Interferometry [13, 34]	Dynamic Interferometry [10, 34, 40]	Dyn. Het. Interferometry (Proposed)
Acquisition Time ^a	4 Measurements	Single Shot	Single Shot
Ambient Light	Resistant	Not Resistant	Resistant
Rapid ^b Mechanical Disturbance	Not Resistant	Not Resistant	Not Resistant

^a Single shot measurement relatively more robust to vibrations.

^b Interferometry is not robust to macroscopic mechanical disturbance.

a heterodyne interferometer has opposite circular polarizations. A linear polarization analyzer, placed in front of a photodetector, shifts the phase between reference and sample wavefronts, and therefore induces a temporal phase shift in the beat signal. The phase is extracted after temporally correlating the beat signal with a known reference.

Table 1 summarizes the scope of DHI. For a feasibility study, DHI is experimentally demonstrated here using commercially available imaging hardware, including a video camera having a polarization mosaic. The mosaic allows the camera to acquire four linear polarization states in a single shot. In future work, high-speed analog lock-in cameras (like the Helicam C3 [1]) could be modified at the device level to achieve polarization multiplexing. Fabrication of this new device would equip DHI with snapshot performance.

Relation to prior art: The phase shifting properties of opposing circularly polarized beams have been previously described and demonstrated [19, 27]. Since then, various polarization phase shifting techniques have been proposed in different interferometric settings, such as homodyne interferometry [10, 40], phase unwrapping [46], fringe projection imaging [41] and shearography [25, 35]. Our goals

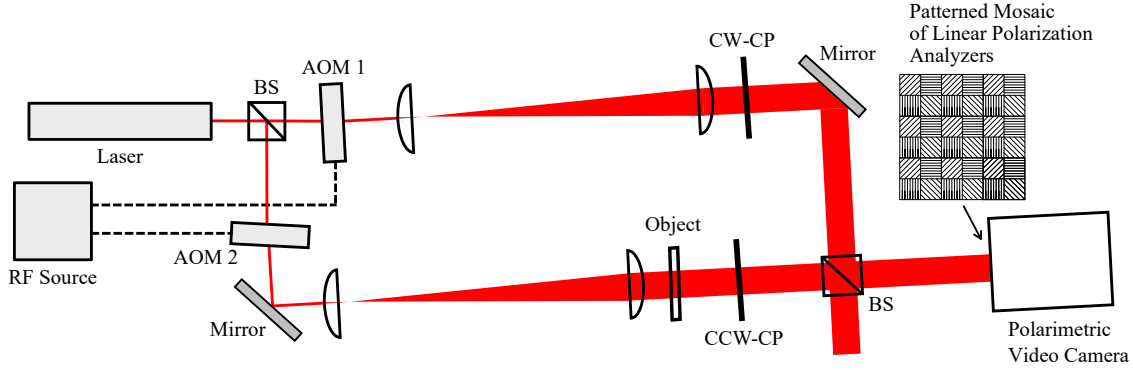


Figure 1: **Schematic of a wide-field implementation of dynamic heterodyne interferometry.** The imaging sensor is a polarimetric camera with a patterned mosaic of linear polarization analyzers placed over the sensor. Such a camera allows four analyzer angles to be sampled in a single image frame. Since the polarimetric camera is limited to video framerates of 30 Hz, two acousto-optic modulators are used to provide a 1 Hz frequency beat note. To emulate a lock-in camera, one pixel on the camera sensor is used as the correlating reference in post-processing. An object is placed in one arm of the interferometer (sample arm), while the other arm is a reference.

are similar (to recover the phase), but we study the scenarios in which time-correlation improves the performance of polarimetric phase shifting. The relatively recent availability of snapshot correlation cameras and snapshot polarimetric cameras motivates our study. Correlation cameras perform on-chip correlation at high (KHz or MHz) frequencies [2, 12, 28, 38]. Polarimetric cameras multiplex multiple linear polarizer rotations in a single image acquisition [3, 4, 9, 11, 15, 17, 26, 39, 45]. Our work benefits from connections to recent works in computational photography, dealing with wave optics [6, 14, 16, 21, 29, 30, 47], polarization [22, 23, 32, 43], and time of flight imaging [7, 18, 20, 24, 37, 48]. As just one such example, computational self-calibration [42] can remove angular inconsistencies between sampled polarimetric data. This could benefit DHI in the future.

2. Dynamic Heterodyne Interferometry

Consider the wide-field setup illustrated in Figure 1. Acousto-optic modulators AOM1 and AOM2 create a temporal beat signal. Let Ω_1 and Ω_2 be the frequency shift created by AOM1 and AOM2, respectively. It will be assumed that the context hereafter is heterodyne interferometry, where $\Omega_1 \neq \Omega_2$.

To establish notation, let us first ignore polarization effects for the moment. In such case, the fields in each arm would be written as

$$\begin{aligned} E_1(\mathbf{x}, t) &= A_1(\mathbf{x}) \exp \left\{ j \left[(\omega + \Omega_1)t + \phi_1(\mathbf{x}) \right] \right\} \\ E_2(\mathbf{x}, t) &= A_2(\mathbf{x}) \exp \left\{ j \left[(\omega + \Omega_2)t + \phi_2(\mathbf{x}) \right] \right\}, \end{aligned} \quad (1)$$

where $j = \sqrt{-1}$ and $E_1(\mathbf{x}, t)$ and $E_2(\mathbf{x}, t)$ represent electric fields in coordinates of space \mathbf{x} and time t . Variables

$A_1(\mathbf{x})$ and $A_2(\mathbf{x})$ represent spatially varying amplitudes, $\phi_1(\mathbf{x})$ and $\phi_2(\mathbf{x})$ represent spatially varying phases, and ω represents the optical frequency. When the two fields interfere, a photodetector observes a temporal beat signal with frequency $\Delta\Omega$ and phase $\Delta\phi(\mathbf{x})$, where

$$\Delta\Omega = \Omega_1 - \Omega_2 \quad \text{and} \quad \Delta\phi(\mathbf{x}) = \phi_1(\mathbf{x}) - \phi_2(\mathbf{x}). \quad (2)$$

Equations (1) and (2) underpin heterodyne interferometry [13, 33], where the goal is to estimate $\Delta\phi(\mathbf{x})$.

Now, we consider polarization effects. The field in each arm passes through a circular polarizer with opposite handedness (cf. elements CW-CP and CCW-CP in Figure 1).¹ The fields in the interferometer are expressed by the following Jones vectors:

$$\begin{aligned} \mathbf{E}_1(\mathbf{x}, t) &= A_1(\mathbf{x}) \exp \left\{ j \left[(\omega + \Omega_1)t + \phi_1(\mathbf{x}) \right] \right\} \begin{pmatrix} 1 \\ j \end{pmatrix} \\ \mathbf{E}_2(\mathbf{x}, t) &= A_2(\mathbf{x}) \exp \left\{ j \left[(\omega + \Omega_2)t + \phi_2(\mathbf{x}) \right] \right\} \begin{pmatrix} 1 \\ -j \end{pmatrix}. \end{aligned} \quad (3)$$

As shown in Figure 1, a polarization mosaic patterned by four linear polarization analyzers is placed on the camera sensor. It is assumed that the mosaic is sufficiently dense, such that the four linear polarization analyzers effectively map to the same resolvable spatial location \mathbf{x} . This is a sensor array in use in dynamic interferometry [10]. We now

¹Slight ellipticity may occur in the circular polarization state of each beam, after any circular polarizer. This occurs if the circular polarizer is not matched to the acousto-optic shifted frequencies $\omega + \Omega_1$ and $\omega + \Omega_2$. In our experiments, the frequency shift is miniscule with respect to the optical frequency, i.e., $\Omega_1/\omega \approx \Omega_2/\omega \approx 10^{-8}$. We thus find the error due to ellipticity to be negligible.

Table 2: Comparison of the equations associated with interferometry techniques.

Heterodyne	$I(\mathbf{x}, t) = A_1(\mathbf{x})A_2(\mathbf{x}) \cos[\Delta\Omega t + \Delta\phi(\mathbf{x})] + A_1^2(\mathbf{x})/2 + A_2^2(\mathbf{x})/2$
Dynamic	$I(\mathbf{x}, \alpha) = A_1(\mathbf{x})A_2(\mathbf{x}) \cos[\Delta\phi(\mathbf{x}) + 2\alpha] + A_1^2(\mathbf{x})/2 + A_2^2(\mathbf{x})/2$
Dynamic Heterodyne	$I(\mathbf{x}, t, \alpha) = A_1(\mathbf{x})A_2(\mathbf{x}) \cos[\Delta\Omega t + \Delta\phi(\mathbf{x}) + 2\alpha] + A_1^2(\mathbf{x})/2 + A_2^2(\mathbf{x})/2$

derive how one particular orientation of a linear polarization analyzer, denoted by the variable α , affects the interference pattern. The fields passing through a linear polarization analyzer are written as a Jones product:

$$\begin{aligned} \mathbf{E}'_1(\mathbf{x}, t) &= \mathbf{J}_\alpha \mathbf{E}_1(\mathbf{x}, t) \\ \mathbf{E}'_2(\mathbf{x}, t) &= \mathbf{J}_\alpha \mathbf{E}_2(\mathbf{x}, t), \end{aligned} \quad (4)$$

where $\mathbf{E}'_1(\mathbf{x}, t)$ and $\mathbf{E}'_2(\mathbf{x}, t)$ denote the fields after the analyzer and \mathbf{J}_α is the Jones matrix for the linear polarization analyzer, where

$$\mathbf{J}_\alpha = \begin{pmatrix} \cos^2 \alpha & \cos \alpha \sin \alpha \\ \sin \alpha \cos \alpha & \sin^2 \alpha \end{pmatrix}. \quad (5)$$

Substituting Equations (3) and (5) into Equation (4) yields

$$\begin{aligned} \mathbf{E}'_1(\mathbf{x}, t) &= A_1(\mathbf{x}) \exp \left\{ j \left[(\omega + \Omega_1)t + \phi_1(\mathbf{x}) + \alpha \right] \right\} \begin{pmatrix} \cos \alpha \\ \sin \alpha \end{pmatrix} \\ \mathbf{E}'_2(\mathbf{x}, t) &= A_2(\mathbf{x}) \exp \left\{ j \left[(\omega + \Omega_2)t + \phi_2(\mathbf{x}) - \alpha \right] \right\} \begin{pmatrix} \cos \alpha \\ \sin \alpha \end{pmatrix}. \end{aligned} \quad (6)$$

Note that now the polarization analyzer angle α corresponds both to a phase shift of the optical wave and a rotation of the Jones vector.

Time-averaging of a quantity $f(t)$ is written in bracket notation as

$$\langle f(t) \rangle = \frac{1}{T} \int_{t-T/2}^{t+T/2} f(t') dt', \quad (7)$$

where T is the *photosensor integration time*. The image intensity at the camera sensor is a time-average of the superimposed fields, such that

$$I(\mathbf{x}, t, \alpha) = \left\langle \left| \mathbf{E}'_1(\mathbf{x}, t) + \mathbf{E}'_2(\mathbf{x}, t) \right|^2 \right\rangle. \quad (8)$$

Since T is much larger than the optical period, but much smaller than the period of the beat signal, it follows that

$$\begin{aligned} I(\mathbf{x}, t, \alpha) &= A_1(\mathbf{x})A_2(\mathbf{x}) \cos [\Delta\Omega t + \Delta\phi(\mathbf{x}) + 2\alpha] \\ &+ \frac{A_1^2(\mathbf{x})}{2} + \frac{A_2^2(\mathbf{x})}{2}. \end{aligned} \quad (9)$$

The details of this derivation can be found in Appendix A.

Now, it is possible to correlate electronically the intensity signal with a known reference at the beat frequency,

$$R(t) = \cos(\Delta\Omega t). \quad (10)$$

The correlation for analyzer angle α is then

$$\begin{aligned} c(\mathbf{x}, \alpha) &= \lim_{T' \rightarrow \infty} \frac{1}{T'} \int_{-T'/2}^{T'/2} I(\mathbf{x}, t, \alpha) R(t) dt \\ &= \frac{1}{2} A_1(\mathbf{x}) A_2(\mathbf{x}) \cos [2\alpha + \Delta\phi(\mathbf{x})], \end{aligned} \quad (11)$$

where T' is the *electronic correlation time*. A distinction can be made between the electronic correlation time T' and the photosensor integration time T of Equation (7). While the electronic correlation time is much longer than the period of the beating signal, the photosensor integration time is much shorter, such that

$$T' \gg \frac{2\pi}{\Delta\Omega} \gg T \gg \frac{2\pi}{\omega}. \quad (12)$$

Now, let us use the term *correlogram* to refer to $c(\mathbf{x}, \alpha)$, the correlation at polarization analyzer angle α . Suppose we have $K = 4$ correlograms collected at angles $0, \frac{\pi}{4}, \frac{\pi}{2}, \frac{3\pi}{4}$ of a linear polarization analyzer. A technique analogous to the four phase trick in dynamic interferometry can be used in the context of correlation as

$$\Delta\hat{\phi}(\mathbf{x}) = \arctan \left[\frac{c(\mathbf{x}, \alpha = \frac{3\pi}{4}) - c(\mathbf{x}, \alpha = \frac{\pi}{4})}{c(\mathbf{x}, \alpha = 0) - c(\mathbf{x}, \alpha = \frac{\pi}{2})} \right]. \quad (13)$$

Equations (3) to (13) describe the principle of DHI.

Suppose that to obtain dynamic performance, the data must be acquired within a few milliseconds per phase map snapshot. The ‘‘dynamic’’ nature of DHI is limited by the largest time quantity in Equation (12). This is T' , which cannot be smaller than the period of the beat signal. By using a beat signal having a short period, T' can be small enough to measure dynamic objects.

3. Addressing Phase Bias from Ambient Light

Dynamic interferometry is affected by ambient phase bias, analytically derived and simulated in Section 3.1. In contrast, DHI is resistant to this bias, as we show in Section 3.2.

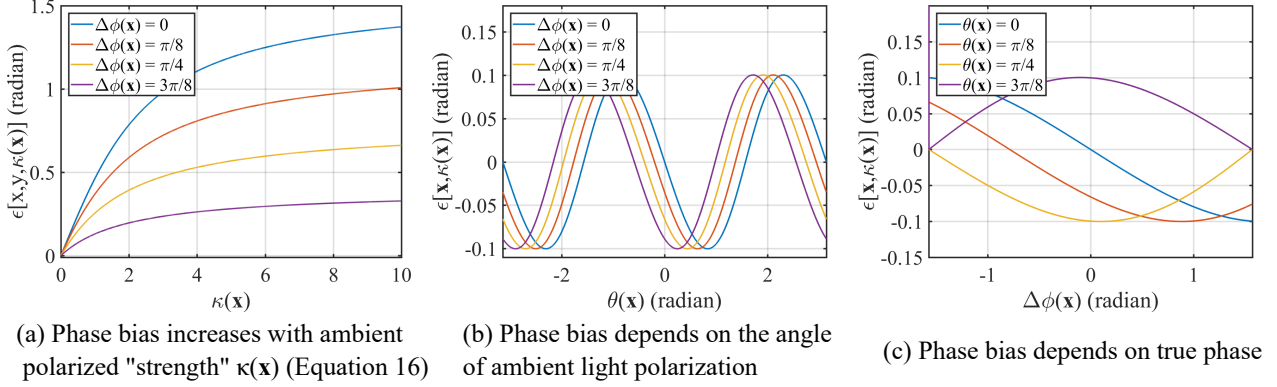


Figure 2: **Ambient phase bias is an undesirable artifact of state-of-the-art techniques [10, 34, 40].** The y-axis for all plots is the difference between the expected, interferometric phase and the measured phase under biased conditions, i.e., $\Delta\phi(\mathbf{x}) - \Delta\phi_{\text{ambient}}(\mathbf{x})$. The angle $\theta(\mathbf{x})$ is fixed at $3\pi/4$ in (a), and $\kappa(\mathbf{x})$ is fixed at 0.2 in (b) and (c).

3.1. Dynamic interferometry under ambient light

In this subsection, we show that the phase recovered from traditional dynamic interferometry is influenced by ambient, partially polarized light. Define $\Gamma(\mathbf{x})$ as the intensity, $\rho(\mathbf{x})$ as the degree of polarization, and $\theta(\mathbf{x})$ as the angle of linear polarization of ambient light. The intensity of ambient light is written as

$$I_{\text{ambient}}(\mathbf{x}, \alpha) = \Gamma(\mathbf{x})[1 - \rho(\mathbf{x})] + \Gamma(\mathbf{x})\rho(\mathbf{x}) \cos^2[\theta(\mathbf{x}) - \alpha]. \quad (14)$$

Assume that ambient light is incoherent, with respect to the interferometer laser. Using Equations (9) and (14), the overall intensity in the presence of ambient light is thus

$$\begin{aligned} \tilde{I}(\mathbf{x}, \alpha) &= I(\mathbf{x}, \alpha) + I_{\text{ambient}}(\mathbf{x}, \alpha) \\ &= A_1(\mathbf{x})A_2(\mathbf{x}) \cos[\Delta\phi(\mathbf{x}) + 2\alpha] \\ &\quad + \frac{A_1^2(\mathbf{x})}{2} + \frac{A_2^2(\mathbf{x})}{2} + \Gamma(\mathbf{x})[1 - \rho(\mathbf{x})] \\ &\quad + \Gamma(\mathbf{x})\rho(\mathbf{x}) \cos^2[\theta(\mathbf{x}) - \alpha], \end{aligned} \quad (15)$$

where $\tilde{I}(\mathbf{x}, \alpha)$ denotes the intensity in the presence of ambient light. To characterize the relative strength of polarized, ambient light, we define a quantity κ , such that

$$\kappa(\mathbf{x}) = \frac{\Gamma(\mathbf{x})\rho(\mathbf{x})}{A_1(\mathbf{x})A_2(\mathbf{x})}. \quad (16)$$

Then, the biased phase estimate from dynamic interferometry is written as

$$\begin{aligned} \Delta\hat{\phi}_{\text{ambient}}(\mathbf{x}) &= \arctan \left[\frac{\tilde{I}(\mathbf{x}, \alpha = \frac{3\pi}{4}) - \tilde{I}(\mathbf{x}, \alpha = \frac{\pi}{4})}{\tilde{I}(\mathbf{x}, \alpha = 0) - \tilde{I}(\mathbf{x}, \alpha = \frac{\pi}{2})} \right] \\ &= \arctan \left[\frac{\sin[\Delta\phi(\mathbf{x})] - \kappa(\mathbf{x}) \sin[2\theta(\mathbf{x})]}{\cos[\Delta\phi(\mathbf{x})] + \kappa(\mathbf{x}) \cos[2\theta(\mathbf{x})]} \right]. \end{aligned} \quad (17)$$

Define the error functional due to bias as

$$\epsilon[\mathbf{x}, \kappa(\mathbf{x})] = \Delta\hat{\phi}_{\text{ambient}}(\mathbf{x}) - \Delta\hat{\phi}(\mathbf{x}). \quad (18)$$

The error depends on the relative strength of polarized, ambient light, as plotted in Figure 2. In an extreme case, when $\kappa(\mathbf{x})$ is large,

$$\lim_{\kappa(\mathbf{x}) \rightarrow \infty} \epsilon[\mathbf{x}, \kappa(\mathbf{x})] = -2\theta(\mathbf{x}) - \Delta\phi(\mathbf{x}). \quad (19)$$

To understand the bias at other regimes of $\kappa(\mathbf{x})$, we substitute Equations (13) and (17) into (18); then compute a first-order expansion about $\kappa(\mathbf{x}) = 0$ to obtain

$$\begin{aligned} \epsilon[\mathbf{x}, \kappa(\mathbf{x})] &\approx \kappa(\mathbf{x}) \left. \frac{\partial \Delta\hat{\phi}_{\text{ambient}}[\mathbf{x}, \kappa(\mathbf{x})]}{\partial \kappa(\mathbf{x})} \right|_{\kappa(\mathbf{x})=0} \\ &= \kappa(\mathbf{x}) \sin[-\Delta\phi(\mathbf{x}) - 2\theta(\mathbf{x})]. \end{aligned} \quad (20)$$

In regimes where $\kappa(\mathbf{x}) \rightarrow 0$, it can be seen that $\epsilon[\mathbf{x}, \kappa(\mathbf{x})] \rightarrow 0$. When $\kappa(\mathbf{x})$ is non-zero and finite, the first-order error is determined by three parameters: $\kappa(\mathbf{x})$, $\theta(\mathbf{x})$, and $\Delta\phi(\mathbf{x})$. When $\Delta\phi(\mathbf{x}) = -2\theta(\mathbf{x})$, the bias is zero. The bias varies sinusoidally with $2\theta(\mathbf{x})$ otherwise. The plots in Figure 2a-c substantiate this analysis.

3.2. DHI's robustness to ambient light

In this subsection, we show that DHI is resistant to ambient phase bias. Intuitively, ambient light does not have significant energy at the heterodyne frequency. To show this analytically, Equation (15) is parametrized in the context of time as

$$\begin{aligned} \tilde{I}(\mathbf{x}, t, \alpha) &= A_1(\mathbf{x})A_2(\mathbf{x}) \cos[\Delta\Omega t + \Delta\phi(\mathbf{x}) + 2\alpha] \\ &+ \frac{A_1^2(\mathbf{x})}{2} + \frac{A_2^2(\mathbf{x})}{2} + \Gamma(\mathbf{x}, t)[1 - \rho(\mathbf{x}, t)] \\ &+ \Gamma(\mathbf{x}, t)\rho(\mathbf{x}, t) \cos^2[\theta(\mathbf{x}, t) - \alpha], \end{aligned} \quad (21)$$

For clarity of derivation, we will assume that the ambient term is steady-state, or DC, with respect to the electronic correlation time. For the moment, consider an idealized correlogram in the presence of ambient light as

$$\begin{aligned} \tilde{c}(\mathbf{x}, \alpha) &= \lim_{T' \rightarrow \infty} \frac{1}{T'} \int_{-T'/2}^{T'/2} \tilde{I}(\mathbf{x}, t, \alpha) R(t) dt \\ &= c(\mathbf{x}, \alpha) + \lim_{T' \rightarrow \infty} \frac{1}{T'} \int_{-T'/2}^{T'/2} I_{\text{ambient}}(\mathbf{x}, \alpha) R(t) dt. \end{aligned} \quad (22)$$

Equation (22) assumes that the correlation time T' is taken to an infinite limit. This simplification is mathematically convenient, but may need to be reconsidered when the correlation time is short and the ambient intensity is high. In this case, we rewrite the last line of Equation (22) as

$$\tilde{c}(\mathbf{x}, \alpha) = c(\mathbf{x}, \alpha) + \frac{1}{T'} \int_{-T'/2}^{T'/2} I_{\text{ambient}}(\mathbf{x}, \alpha) R(t) dt, \quad (23)$$

where we have removed the limit notation from the ambient term only (since we are studying ambient bias effects). Now, let $R(t)$ take the form given in Equation (10). Then it follows that

$$\tilde{c}(\mathbf{x}, \alpha) = c(\mathbf{x}, \alpha) + \frac{I_{\text{ambient}}(\mathbf{x}, \alpha)}{T'} \int_{-T'/2}^{T'/2} \cos(\Delta\Omega t) dt, \quad (24)$$

which allows the effect of ambient light on the correlation to be lower bounded as

$$|\tilde{c}(\mathbf{x}, \alpha) - c(\mathbf{x}, \alpha)| \leq \frac{2I_{\text{ambient}}(\mathbf{x}, \alpha)}{\Delta\Omega T'}. \quad (25)$$

We will provide the derivation assuming that the ambient bias is positive. Then, the biased estimate in the context of

correlation is

$$\begin{aligned} \Delta\hat{\phi}_{\text{ambient}}(\mathbf{x}) &= \arctan \left[\frac{\tilde{c}(\mathbf{x}, \alpha = 3\pi/4) - \tilde{c}(\mathbf{x}, \alpha = \pi/4)}{\tilde{c}(\mathbf{x}, \alpha = 0) - \tilde{c}(\mathbf{x}, \alpha = \pi/2)} \right] \\ &= \arctan \left[\frac{\sin[\Delta\phi(\mathbf{x})] - \kappa(\mathbf{x}) \sin[2\theta(\mathbf{x})] \frac{2}{\Delta\Omega T'}}{\cos[\Delta\phi(\mathbf{x})] + \kappa(\mathbf{x}) \cos[2\theta(\mathbf{x})] \frac{2}{\Delta\Omega T'}} \right]. \end{aligned} \quad (26)$$

In analogy to Section 3.1, we can use a first-order expansion to express the bias as

$$\epsilon[\mathbf{x}, \kappa(\mathbf{x})] \approx \frac{2}{\Delta\Omega T'} \kappa(\mathbf{x}) \sin[-\Delta\phi(\mathbf{x}) - 2\theta(\mathbf{x})]. \quad (27)$$

Compared to Equation (20), the bias is attenuated by $\frac{2}{\Delta\Omega T'}$. From Equation (12) it can be seen that

$$\frac{2}{\Delta\Omega T'} \ll 1. \quad (28)$$

Hence dynamic heterodyne interferometry is more resistant to partially polarized ambient light, than traditional dynamic interferometry.

Concrete example: The resonant frequency of an Isomet 1205C-2 acousto-optic modulator is 80 MHz. The Stanford SR850 lock-in amplifier has an adjustable correlation time, with a midrange value of 3 milliseconds. Then the bias attenuation is

$$\begin{aligned} \frac{2}{\Delta\Omega T'} &= \frac{2}{(2\pi \times 80 \times 10^6 \text{ Hz})(3 \times 10^{-3} \text{ sec})} \\ &= 1.33 \times 10^{-6}. \end{aligned} \quad (29)$$

Regarding shot noise: The performance of DHI in shot noise conditions parallels that of heterodyne interferometry. Analysis of shot noise in heterodyne interferometers has been previously studied by Niebauer et al. [36] where it is concluded that heterodyne interferometers (like DHI) are in general slightly more sensitive to shot noise. The insights from [36] frame our simulation in Figure 3, where photon noise is modeled as a Poisson process.

4. Assessment and Results

Simulations and an experimental prototype validate the analytical derivations.

Simulation using a computer graphics renderer: A scene of a screw thread is generated using a computer graphics rendering program. A photographic rendering of the synthetic scene is shown in the upper-left of Figure 3. We simulate the forward measurements of both dynamic heterodyne interferometry and dynamic interferometry at

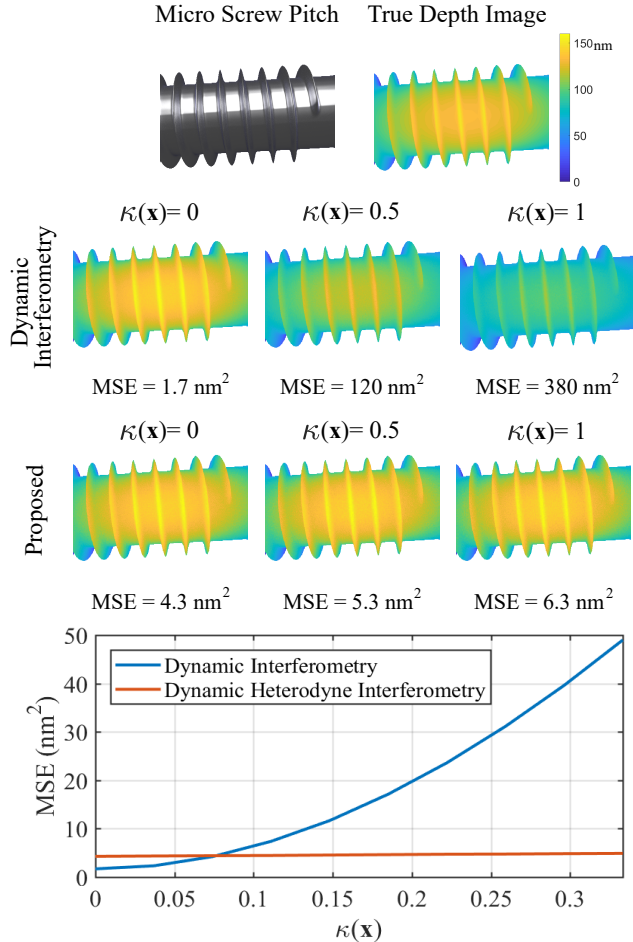


Figure 3: **The proposed technique is more resistant to ambient bias than prior art [10] (simulated result).** The rendered scene, screw pitch with 150nm depth, is captured with a reflection-mode interferometer. Ambient light is assumed to have partial linear polarization, where the polarization angle is $\theta(\mathbf{x}) = 0$.

varying levels of ambient, partially polarized light. The simulation model assumes a shot-noise limited scenario. As the ambient strength $\kappa(\mathbf{x})$ increases, the error increases in a 3D reconstruction derived by traditional dynamic interferometry. In comparison, DHI can capture an accurate depth image with increasing strength of polarized ambient light. The plot shows the mean squared error between the true and recovered depths. Note that our simulation accounts for non-stationary shot noise [36]. Hence, in the presence of zero ambient light, DHI performs slightly worse than traditional dynamic interferometry.

Experimental implementation: Hereafter, we consider experimental results. To illustrate feasibility, we demonstrate wide-field DHI by operating a polarimetric camera in video mode. The schematic used for the experiments

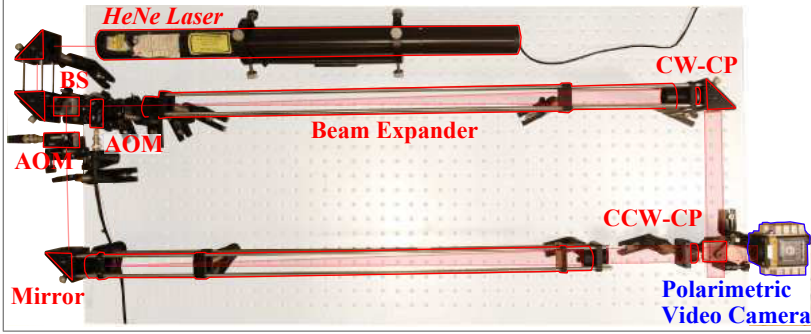
is illustrated in Figure 1 with a photograph of the implementation shown in Figure 4. The polarimetric camera we used is the PolarCam from 4D technologies and has a pixelated polarization mosaic to sample four linear polarization states in one snapshot [3]. A dual-channel RF signal generator drives the acousto-optic modulators at frequencies of $\Omega_1 = 80\text{MHz}$ and $\Omega_2 = 80\text{MHz} + 1\text{Hz}$, based on two design principles: (1) Ω_1 and Ω_2 must operate near the AOM resonance frequency (specified at 80 MHz); and (2) the beat note $\Delta\Omega$ must be within the framerate of the polarimetric video camera. Choosing frequencies that violate condition (1) would result in low modulation depth. Since we use a video camera, the electronic correlation time that was chosen was $T' = 6$ seconds, while the photosensor integration time was $T = 0.5$ milliseconds. Appendix B describes the mechanics of obtaining correlograms from this polarimetric video camera. Beam expanders in each arm widen the beam to 25.4 mm. A measurement is taken by placing an object into one of the arms of the interferometer. The values of constants used to generate experimental data are contained in Table 3.

Table 3: **Experimental constants for Figs. 6 and 7.**

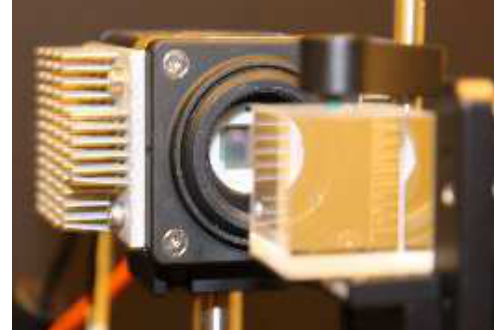
	Description	Unit	Experimental Value
ω	Optical Frequency	Hz	$4.74 \cdot 10^{14}$
Ω_1	AOM1 Frequency	MHz	80
Ω_2	AOM2 Frequency	MHz	80.000001
$\Delta\Omega$	Beat Frequency	Hz	1
α	Analyzer Angle	radian	$0, \pi/4, \pi/2, 3\pi/4$
T'	Correlation Time	s	6
T	Integration Time	ms	0.5

Experimental validation of the forward model: We aim to validate that according to Equation (9), a rotation of the linear polarization analyzer by an angle of α shifts the phase between reference and sample wavefronts by 2α . This wavefront shift is predicted to manifest as a temporal phase delay in the measured, temporal beat signal. We validate this principle by rotating a linear polarizer in front of a photodiode. Figure 5 shows the plot of the linear polarizer angle versus observed phase shift in the measured beat note. The experimental result is consistent with our analytical prediction.

Space-time-polarization fringe: The interferometer generates a spatial fringe pattern. Since we introduce a beat note, the fringe pattern is also time-varying. Video captured by the PolarCam exhibits polarization-dependent phase shifting in time. Hence, the fringe is space, time, and polarization dependent. A video of this unique fringe pattern, in ideal conditions without ambient light bias, can be found at [5].



(a) Set Up Overview



(b) Polarimetric Video Camera

Figure 4: **Experimental setup.** (a) Overview of the setup with the beam path and hardware. (b) Inset of the pixelated polarization camera, which simultaneously captures images of four different linear polarization analyzer states.

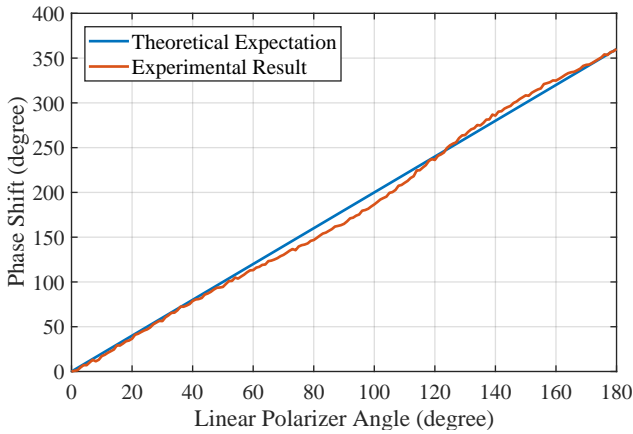


Figure 5: **Experimental evaluation is consistent with theoretical prediction.** The unwrapped phase shift imparted by the linear polarization analyzer in Equation (9) is consistent with experimental data.

Glass slide scene: We use the same benchmark experimental scene as in previous interferometric work [38]. The scene is a glass slide that covers half of the beam. To demonstrate an advantage of DHI, we performed a comparison with a re-implementation of standard dynamic interferometry (analogous to the setup in [10]). The interferometer is placed in uncontrolled, ambient lighting conditions, which we impose by using an off-the-shelf flashlight. The sample object is a 1.37mm thick glass slide, which again, is a well-known interferometric test scene [38]. As illustrated in Figure 6, the bias from ambient light corrupts the phase measurement from dynamic interferometry. In comparison, the phase measurement from DHI is no different in ambient and controlled conditions.

Water drop scene: We repeat the experiment from the preceding paragraph, now using a water drop placed on a microscope slide. As illustrated in Figure 7b, the ground

truth phase image consists of pathlength variations that occur at a high spatial frequency. The proposed technique of DHI is able to recover an approximation of the ground truth (Figure 7c). While the additional shot noise from ambient light introduces some noise to the DHI reconstruction, the high-frequency variations in pathlength are preserved. However, as shown in Figure 7d, the previous technique of [10] is not able to recover high-frequency variations in pathlength; instead, the phase image is overwhelmed by low-frequency bias due to ambient light.

5. Discussion and Conclusion

In summary, DHI is shown to be resistant to phase bias. Experimental results substantiate the applicability of our analytical derivations.

The proof-of-concept we have demonstrated was only for the purpose of testing feasibility and making comparisons with traditional dynamic interferometry. It is not an ideal, industrial implementation. The use of a video framerate imager limits the time-correlation to low-frequency signals. For the results in this paper we used a beat tone of 1 Hertz. Therefore, each cycle has a period of 1 second, which means that acquiring the correlograms takes on the order of seconds. Another limitation of low-frequencies is the difficulty of generating stable, low-frequency beat notes with modulation hardware. The acousto-optic modulators resonate at 80 MHz. Since the frequency difference between the two modulators is 1 Hertz, the beat frequency requires a stability in frequency of less than one part per million.

As a fusion technique, DHI is susceptible to the joint limitations of polarimetric and heterodyne approaches. This includes the additional complexity, tradeoff of spatial resolution for time resolution, as well as classic heterodyne challenges like frequency drift and spurious resonance in peripheral electronics. Pertaining to this latter point, we adopted techniques like EMI shielding of cables (to avoid

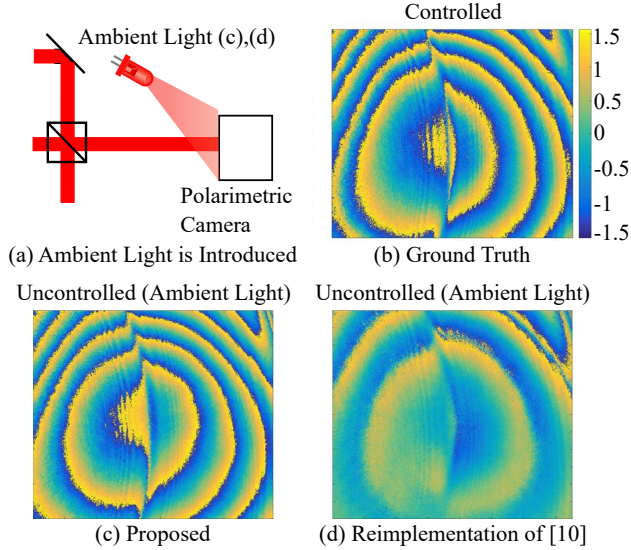


Figure 6: **The proposed technique is more resistant to ambient bias than prior art [10] (experimental result).** (a) Ambient bias is introduced by turning on a consumer flashlight in the optical laboratory (with unknown polarization). (b) The target phase image is obtained without the ambient flashlight. (c) The proposed approach closely approximates the target surface. (d) The traditional approach [10] is unsuccessful.

noise at the heterodyne frequency) and adoption of resonant frequency modulation of the AOMs.

To obtain snapshot performance comparable to dynamic interferometry, we would need a specialized device: a polarimetric correlation camera. An ordinary correlation camera is designed to correlate an optical signal at KHz or MHz frequencies with an on-chip electronic reference. The photonic mixer device is one such example [2]. In the context of DHI, correlation cameras increase the allowable beat frequency ($\Delta\Omega$) to KHz or MHz ranges. Hence, from Equation (12), the correlation time (T') can be on the order of a millisecond. While correlation cameras are available off-the-shelf, none of the current devices spatially sample different polarization states. Hence, it would be necessary to fabricate a new device to realize the full benefits of DHI. Figure 8 illustrates a potential design architecture for DHI.

Potential alternatives: We have recasted heterodyne interferometry into a polarimetric context to spur dynamic performance. However, alternate strategies for dynamic performance could be considered in future work. For instance, it should be possible to add a phase-shifting spatial light modulator (SLM) to a heterodyne interferometer. This hypothetical technique can be seen as an extension of [31]. It is anticipated that alignment challenges would occur when the SLM pixel size is unmatched to the camera

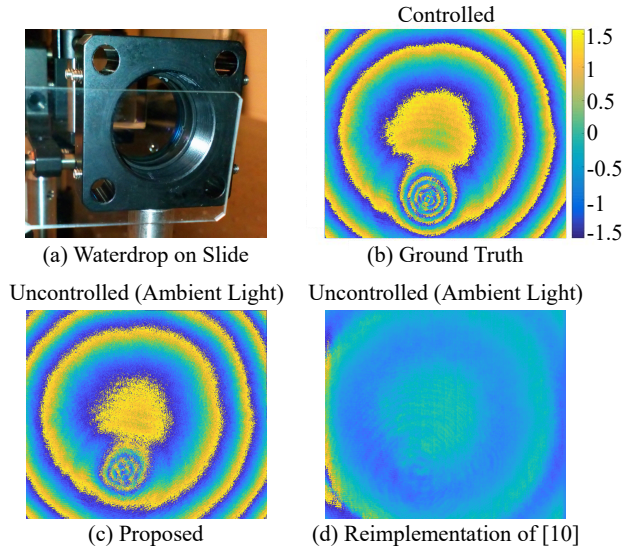


Figure 7: **Comparisons on a more complex scene (experimental result)** (a) A water droplet on the glass slide introduces phase shift due to its curvature and refractive index. (b) The target phase image is obtained without the ambient flashlight. (c) The proposed approach approximates the target phase image. (d) The traditional approach [10] fails to recover the water drop's phase.

(as is usually the case). A brute force engineering strategy could opt for short exposures and a mirror capable of rapid translation. In the context of alternatives, we believe that the use of polarization represents one of the simplest experimental methods of realizing DHI.

Conclusion: We hope that the results of this investigation motivate: (1) future device-level fabrication of a multipolar PMD camera, shown in Figure 8, that operates in high-frequency; (2) new pathways for field interferometry; and (3) further mathematical unity of polarization and time-resolved phenomena.

Acknowledgments

The authors thank Anat Levin, Bergin Gjonaj, Guy Bartal from the Technion and Mickey McDonald from Columbia University for useful discussions. AK was supported by the Rahahimmoff Award (Israel-United States Binational Science Foundation T-2015-227), the Charles Draper Doctoral Fellowship, and the Qualcomm Innovation Fellowship. YYS is a Landau Fellow - supported by the Taub Foundation. His work in this project is supported by the Israel Science Foundation (Grant 542/16). The research was partly carried in the Ollendorff Minerva Center. Minerva is funded through the BMBF. The work of all MIT-affiliated authors was supported by the Media Lab consortium funding.

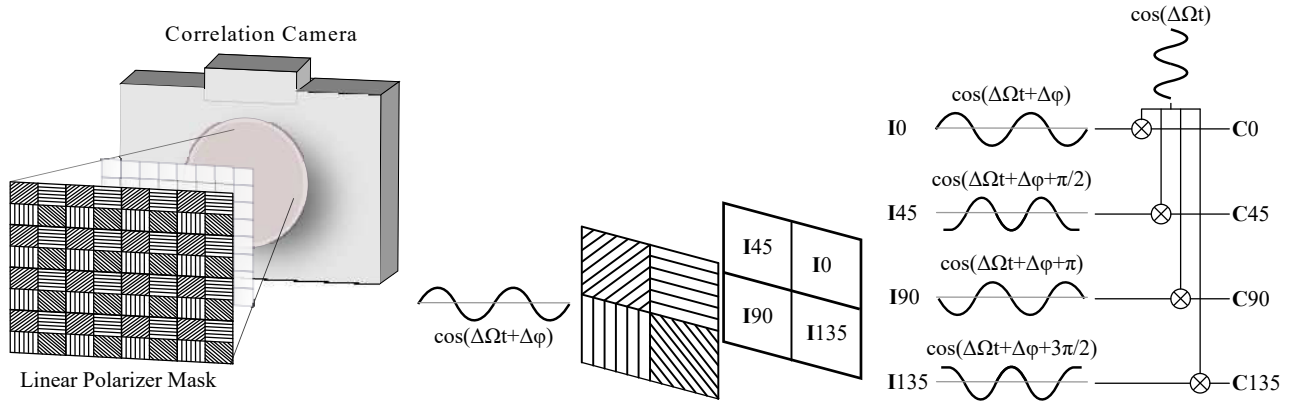


Figure 8: **Motivating future imaging chip design.** To leverage snapshot performance, the proposed technique should be implemented on a polarimetric correlation camera (essentially, a PMD camera with a pixelated polarizer array). (left) Correlating pixels are placed behind a tiled mask of linear polarization analyzers (akin to a Bayer mask). (right) Phase is estimated using the approach we describe in this paper.

References

- [1] <http://www.heliotis.ch/downloads/C3DS.pdf>. Online.
- [2] <http://www.pmdtec.com/index.php>. Online.
- [3] <https://www.4dtechnology.com/products/polarimeters/polarcam/>. Online.
- [4] <http://www.fluxdata.com/products/fd-1665p>. Online.
- [5] <https://youtu.be/KXMg9Pc6eL8>. Online.
- [6] N. Antipa, S. Necula, R. Ng, and L. Waller. Single-shot diffuser-encoded light field imaging. In *IEEE International Conference on Computational Photography (ICCP)*, pages 1–11, May 2016.
- [7] J. Bai, M. Chandraker, T.-T. Ng, and R. Ramamoorthi. A dual theory of inverse and forward light transport. In *Proceedings of the 11th European Conference on Computer Vision: Part II, ECCV*, pages 294–307, 2010.
- [8] A. Bhandari and R. Raskar. Signal processing for time-of-flight imaging sensors: An introduction to inverse problems in computational 3-d imaging. *IEEE Signal Processing Magazine*, 33(5):45–58, 2016.
- [9] N. J. Brock, C. Crandall, and J. E. Millerd. Snap-shot imaging polarimeter: performance and applications. In *Proc. SPIE, Polarization: Measurement, Analysis, and Remote Sensing XI*, volume 9099, 2014.
- [10] N. J. Brock, J. B. Hayes, B. Kimbrough, J. E. Millerd, M. North-Morris, M. Novak, and J. C. Wyant. Dynamic interferometry. In *Proc. SPIE, Novel Optical Systems Design and Optimization VIII*, volume 5875, 2005.
- [11] N. J. Brock, J. E. Millerd, J. C. Wyant, and J. B. Hayes. Pixelated phase-mask interferometer, August 2003. US Patent US7230717B2.
- [12] B. Buttgen and P. Seitz. Robust optical time-of-flight range imaging based on smart pixel structures. *IEEE Trans. Circuits and Syst.*, 55(6):1512–1525, 2008.
- [13] J. Chen, Y. Ishii, and K. Murata. Heterodyne interferometry with a frequency-modulated laser diode. *Appl. Opt.*, 27(1):124–128, 1988.
- [14] O. Cossairt, N. Matsuda, and M. Gupta. Digital refocusing with incoherent holography. In *IEEE International Conference on Computational Photography (ICCP)*, pages 1–9, May 2014.
- [15] D. J. Diner, A. Davis, B. Hancock, G. Gutt, R. A. Chipman, and B. Cairns. Dual-photoelastic-modulator-based polarimetric imaging concept for aerosol remote sensing. *Appl. Opt.*, 46(35):8428–8445, 2007.
- [16] I. Gkioulekas, A. Levin, F. Durand, and T. Zickler. Micron-scale light transport decomposition using interferometry. *ACM Trans. Graph.*, 34(4):37:1–37:14, 2015.
- [17] V. Gruev, A. Ortu, N. Lazarus, J. Van der Spiegel, and N. Engheta. Fabrication of a dual-tier thin film micropolarization array. *Opt. Express*, 15(8):4994–5007, 2007.
- [18] F. Heide, M. B. Hullin, J. Gregson, and W. Heidrich. Low-budget transient imaging using photonic mixer devices. *ACM Trans. Graph.*, 32(4):45, 2013.
- [19] H. Z. Hu. Polarization heterodyne interferometry using a simple rotating analyzer. 1: Theory and error analysis. *Appl. Opt.*, 22(13):2052–2056, 1983.
- [20] A. Jarabo, J. Marco, A. Munoz, R. Buisan, W. Jarosz, and D. Gutierrez. A framework for transient rendering. *ACM Trans. Graph.*, 33(6), November 2014.
- [21] A. Kadambi and R. Raskar. Rethinking machine vision time of flight with ghz heterodyning. *IEEE Access*, 2017.
- [22] A. Kadambi, V. Taamazyan, B. Shi, and R. Raskar. Polarized 3d: High-quality depth sensing with polarization cues. In *in Proceedings of the IEEE International Conference on Computer Vision*, pages 3370–3378, 2015.
- [23] A. Kadambi, V. Taamazyan, B. Shi, and R. Raskar. Depth sensing using geometrically constrained polarization normals. *Int. J. Computer Vision*, pages 1–18, 2017.

- [24] A. Kadambi, R. Whyte, A. Bhandari, L. Streeter, C. Barsi, A. Dorrington, and R. Raskar. Coded time of flight cameras: Sparse deconvolution to address multipath interference and recover time profiles. *ACM Trans. Graph.*, 32(6):167:1–167:10, Nov. 2013.
- [25] S.-G. Kim. Polarization phase-shifting technique in shearographic system with a wollaston prism. *J. Opt. Soc. Korea*, 8(3):122–126, 2004.
- [26] B. Kimbrough. Correction of errors in polarization based dynamic phase shifting interferometers. *International Journal of Optomechatronics*, 8(4):304–312, 2014.
- [27] M. P. Kothiyal and C. Delisle. Optical frequency shifter for heterodyne interferometry using counterrotating wave plates. *Opt. Lett.*, 9(8):319–321, 1984.
- [28] R. Lange and P. Seitz. Solid-state time-of-flight range camera. *IEEE J. Quantum Electronics*, 37(3):390–397, 2001.
- [29] A. Levin, D. Glasner, Y. Xiong, F. Durand, W. Freeman, W. Matusik, and T. Zickler. Fabricating brdfs at high spatial resolution using wave optics. *ACM Trans. Graph.*, 32(4):144:1–144:14, July 2013.
- [30] F. Li, J. Yablou, A. Velten, M. Gupta, and O. Cossairt. High-depth-resolution range imaging with multiple-wavelength superheterodyne interferometry using 1550-nm lasers. *Appl. Opt.*, 56(31):H51–H56, 2017.
- [31] M. Lin, K. Nitta, O. Matoba, and Y. Awatsuji. Parallel phase-shifting digital holography with adaptive function using phase-mode spatial light modulator. *Appl. Opt.*, 51(14):2633–2637, May 2012.
- [32] A. Manakov, J. Restrepo, O. Klehm, R. Hegedus, E. Eisele, H.-P. Seidel, and I. Ihrke. A reconfigurable camera add-on for high dynamic range, multispectral, polarization, and light-field imaging. *ACM Trans. Graph.*, 32(4):47:1–47:14, 2013.
- [33] M. McDonald, J. Ha, B. H. McGuyer, and T. Zelevinsky. Visible optical beats at the hertz level. *Am. J. Phys.*, 82(10):1003–1005, 2014.
- [34] C. Meneses-Fabian and U. Rivera-Ortega. Phase-shifting interferometry by amplitude modulation. In *Interferometry-Research and Applications in Science and Technology*. In-Tech, 2012.
- [35] V. Murukeshan, O. L. Seng, and A. Asundi. Polarization phase shifting shearography for optical metrological applications. *Opt. Laser Technol.*, 30(8):527–531, 1998.
- [36] T. M. Niebauer, R. Schilling, K. Danzmann, A. Rüdiger, and W. Winkler. Nonstationary shot noise and its effect on the sensitivity of interferometers. *Phys. Rev. A*, 43:5022–5029, May 1991.
- [37] M. O’Toole, R. Raskar, and K. N. Kutulakos. Primal-dual coding to probe light transport. *ACM Trans. Graph.*, 31(4):39:1–39:11, 2012.
- [38] R. Patel, S. Achamfuo-Yeboah, R. Light, and M. Clark. Widefield heterodyne interferometry using a custom cmos modulated light camera. *Opt. Express*, 19(24):24546–24556, 2011.
- [39] J. L. Pezzaniti and D. B. Chenault. A division of aperture mwir imaging polarimeter. In *Proc. SPIE, Polarization Science and Remote Sensing II*, volume 5888, 2005.
- [40] G. Rodriguez-Zurita, C. Meneses-Fabian, N.-I. Toto-Arellano, J. F. Vázquez-Castillo, and C. Robledo-Sánchez. One-shot phase-shifting phase-grating interferometry with modulation of polarization: case of four interferograms. *Opt. Express*, 16(11):7806–7817, 2008.
- [41] B. Salahieh, Z. Chen, J. J. Rodriguez, and R. Liang. Multi-polarization fringe projection imaging for high dynamic range objects. *Opt. Express*, 22(8):10064–10071, 2014.
- [42] Y. Y. Schechner. Self-calibrating imaging polarimetry. In *Proceedings of IEEE International Conference on Computational Photography*, pages 1–10, 2015.
- [43] Y. Y. Schechner, S. G. Narasimhan, and S. K. Nayar. Instant dehazing of images using polarization. In *Proceedings of IEEE Conference on Computer Vision and Pattern Recognition*, volume 1, pages 325–332, 2001.
- [44] H. Schreiber and J. H. Bruning. Phase shifting interferometry. *Optical Shop Testing, Third Edition*, pages 547–666, 2006.
- [45] J. S. Tyo, D. L. Goldstein, D. B. Chenault, and J. A. Shaw. Review of passive imaging polarimetry for remote sensing applications. *Appl. Opt.*, 45(22):5453–5469, 2006.
- [46] H. Van Brug. Temporal phase unwrapping and its application in shearography systems. *Appl. Opt.*, 37(28):6701–6706, 1998.
- [47] L. Waller, L. Tian, and G. Barbastathis. Transport of intensity phase-amplitude imaging with higher order intensity derivatives. *Opt. Express*, 18(12):12552–12561, 2010.
- [48] D. Wu, M. O’Toole, A. Velten, A. Agrawal, and R. Raskar. Decomposing global light transport using time of flight imaging. In *IEEE Conference on Computer Vision and Pattern Recognition*, pages 366–373, June 2012.

Appendix A: Deriving the Image Intensity

Here, we derive the intermediate steps to obtain Equation (9). The derivation is algebraic, but we offer it here for convenience. By expanding Equation (4), the two fields after the linear polarization analyzer are written in the form of

$$\begin{aligned}
 \mathbf{E}'_1(\mathbf{x}, t) &= A_1(\mathbf{x}) \exp \left\{ j \left[(\omega + \Omega_1)t + \phi_1(\mathbf{x}) \right] \right\} \\
 &\quad \times \begin{pmatrix} \cos^2 \alpha & \cos \alpha \sin \alpha \\ \sin \alpha \cos \alpha & \sin^2 \alpha \end{pmatrix} \begin{pmatrix} 1 \\ j \end{pmatrix} \\
 &= A_1(\mathbf{x}) \exp \left\{ j \left[(\omega + \Omega_1)t + \phi_1(\mathbf{x}) + \alpha \right] \right\} \\
 &\quad \times \begin{pmatrix} \cos \alpha \\ \sin \alpha \end{pmatrix} \\
 \mathbf{E}'_2(\mathbf{x}, t) &= A_2(\mathbf{x}) \exp \left\{ j \left[(\omega + \Omega_2)t + \phi_2(\mathbf{x}) \right] \right\} \\
 &\quad \times \begin{pmatrix} \cos^2 \alpha & \cos \alpha \sin \alpha \\ \sin \alpha \cos \alpha & \sin^2 \alpha \end{pmatrix} \begin{pmatrix} 1 \\ -j \end{pmatrix} \\
 &= A_2(\mathbf{x}) \exp \left\{ j \left[(\omega + \Omega_2)t + \phi_2(\mathbf{x}) - \alpha \right] \right\} \\
 &\quad \times \begin{pmatrix} \cos \alpha \\ \sin \alpha \end{pmatrix}.
 \end{aligned}$$

(30)

Simplification in Equation (30) was achieved through Euler’s formula. Let $\Re\{\cdot\}$ denote the real part of the electric field. The intensity can now be expressed as

$$\begin{aligned}
I(\mathbf{x}, t, \alpha) &= \left\langle \left[\mathbf{E}'_1(\mathbf{x}, t) + \mathbf{E}'_2(\mathbf{x}, t) \right] \left[\mathbf{E}'_1^*(\mathbf{x}, t) + \mathbf{E}'_2^*(\mathbf{x}, t) \right] \right\rangle \\
&= \left\langle \mathbf{E}'_1(\mathbf{x}, t) \mathbf{E}'_1^*(\mathbf{x}, t) \right\rangle + \left\langle \mathbf{E}'_2(\mathbf{x}, t) \mathbf{E}'_2^*(\mathbf{x}, t) \right\rangle \\
&\quad + 2 \left\langle \Re \left\{ \mathbf{E}'_1(\mathbf{x}, t) \mathbf{E}'_2^*(\mathbf{x}, t) \right\} \right\rangle \\
&= \frac{A_1^2(\mathbf{x})}{2} + \frac{A_2^2(\mathbf{x})}{2} + 2 \Re \left\{ \left\langle \mathbf{E}'_1(\mathbf{x}, t) \mathbf{E}'_2^*(\mathbf{x}, t) \right\rangle \right\}.
\end{aligned} \tag{31}$$

The rightmost term can be simplified using Equation (12), i.e., $T \ll \frac{2\pi}{\Delta\Omega}$. Therefore, the complex exponential corresponding to the heterodyne signal, i.e., $\exp[\Delta\Omega t + \Delta\phi(\mathbf{x}) + 2\alpha]$, is approximately constant during the time average. The intensity can now be simplified to

$$\begin{aligned}
I(\mathbf{x}, t, \alpha) &= \frac{A_1^2(\mathbf{x})}{2} + \frac{A_2^2(\mathbf{x})}{2} \\
&\quad + 2 \Re \left\{ \frac{A_1(\mathbf{x}) A_2(\mathbf{x})}{2} \exp \left[\Delta\Omega t + \Delta\phi(\mathbf{x}) + 2\alpha \right] \right\} \\
&= \frac{A_1^2(\mathbf{x})}{2} + \frac{A_2^2(\mathbf{x})}{2} \\
&\quad + A_1(\mathbf{x}) A_2(\mathbf{x}) \cos \left[\Delta\Omega t + \Delta\phi(\mathbf{x}) + 2\alpha \right],
\end{aligned} \tag{32}$$

which completes the derivation of Equation (9).

Appendix B: Generating Correlograms

We now describe the conversion of polarimetric video streams to correlograms. Although a variety of polarimetric video cameras can be used, we concern ourselves here with a sensing approach like the PolarCam from 4D Technologies [3]. The readout from this camera is a parallel stream of four videos, corresponding to $\{I(\mathbf{x}, t, \alpha_1), I(\mathbf{x}, t, \alpha_2), I(\mathbf{x}, t, \alpha_3), I(\mathbf{x}, t, \alpha_4)\}$.

To obtain the interferometric phase, we must first define a reference signal (cf. Equation (10)). To avoid synchronization issues, our reference signal is the beat signal measured at a “reference pixel” on the same camera. This reference pixel is fixed for the experiment and corresponds to spatial location \mathbf{x}_r . Following from Equation (10), polarization does not factor into the reference signal. How-

ever, since this camera does not have a polarization agnostic channel, we must still choose a polarization channel in defining the reference signal. As such we define $R(t) \triangleq I(\mathbf{x}_r, t, \alpha_1)$, where α_1 was chosen without loss of generality.

With the reference signal defined, we can now process the phase from the i -th “input pixel”, at spatial coordinate, \mathbf{x}_i . The correlogram of the k -th polarization angle is

$$c(\mathbf{x}_i, \alpha_k) = \lim_{T' \rightarrow \infty} \frac{1}{T'} \int_{-T'/2}^{T'/2} I(\mathbf{x}_i, t, \alpha_k) I(\mathbf{x}_r, t, \alpha_1) dt. \tag{33}$$

Denote $\varphi(\mathbf{x}_i) = \Delta\phi(\mathbf{x}_i) - \Delta\phi(\mathbf{x}_r)$ as the relative phase difference observed between the input and reference pixels. In the specific case where $\{\alpha_1, \dots, \alpha_4\}$ are $\pi/4$ radians apart, a four phase trick can be used to estimate $\widehat{\varphi}(\mathbf{x}_i)$ in a manner analogous to Equation (13).

The method discussed in this appendix is one possible approach to obtain the correlograms. One can also use a correlation camera which can operate at KHz or MHz bandwidths (cf. Section 5 and Figure 8).

Appendix C: Reproducibility

To allow others to reproduce our DHI implementation, we provide the list of parts used.

Description	Qty.	Model	Manufacturer
Snapshot polarimetric camera	1	PolarCam	4D Technologies
Acousto-optic modulator	2	1205C-2	ISOMET
1" CW circ. polarizer, 633nm	1	CP1L633	Thorlab
1" CCW circ. polarizer, 633nm	1	CP1R633	Thorlab
Non-polarizing beam splitter	2	BS013	Thorlab
Aluminum mirror	4	PF10-03-F01	Thorlab
1" plano-convex lens, f=25.4mm	2	LA1951	Thorlab
1" plano-convex lens, f=750mm	2	LA1978	Thorlab
HeNe laser, 632.8nm, 20mW	1	HNS-20P-633	Meredith Instruments
Signal generator	1	DG4162	RIGOL Technologies
RF amplifier	2	ZHL-3A+	Mini-Circuits
DC power supply	2	TP3005T	Tekpower
Right-angle mirror mount	4	KCB1	Thorlab
Kinematic mount	4	KM100PM	Thorlab
Clamping arm	4	PM4	Thorlab
1" adjustable lens tube	2	SM1V10	Thorlab
1" lens tube	2	SM1L05	Thorlab
Cage assembly rod, length=24"	6	ER24	Thorlab
Cage assembly rod, length=8"	6	ER8	Thorlab
Cage assembly rod, length=2"	3	ER2	Thorlab